Research article

Assessment of natural radioactivity levels and hazard indicators in Tarakeshwor Municipality, Nepal through in-situ technique and multivariate analysis

Devendra Raj Upadhyay [a,b,*], Anish Phuyal [b], Suffian Mohamad Tajudin [c], Raju Khanal [a]

[a] Central Department of Physics, Tribhuvan University, Kirtipur, Kathmandu, Nepal
[b] Department of Physics, Amrit Campus, Tribhuvan University, Kathmandu, Nepal
[c] Faculty of Health Sciences, Sultan Zainal Abidin University, Terengganu, Malaysia

ARTICLE INFO

ABSTRACT

The evaluation of primordial radionuclide concentrations in rapidly urbanized and concrete-laden areas through the importation of construction materials from various regions of Nepal is both important and essential. This study utilized a portable gamma-ray spectrometer (PGIS 2) to analyze the distribution of three natural radionuclides: uranium (^{238}U), thorium (^{232}Th), and potassium (^{40}K) in Tarakeshwor Municipality, Kathmandu, Nepal. The measured dose rates ranged from 70.22 nSv hr^{-1} to 163.66 nSv hr^{-1}, with an average of 124.65±20.29 nSv hr^{-1}, surpassing the global average of 59 nSv hr^{-1}. The activity concentrations of ^{40}K, ^{238}U, and ^{232}Th exceeded global averages, indicating relatively higher natural radioactivity concentrations in the region. Specifically, the average values for ^{40}K, ^{238}U, and ^{232}Th were 935.26±172.30 Bq kg^{-1}, 80.47±15.53 Bq kg^{-1}, and 80.44±18.58 Bq kg^{-1}, respectively. The calculated radium equivalent (Ra$_{eq}$) ranged from 132.26 to 351.22 Bq kg^{-1}, and the annual gonadal equivalent dose ($AGED$) varied from 372.61 to 1028.81 μSv yr^{-1}. The annual effective dose rates for indoor and outdoor environments were 0.54±0.09 mSv yr^{-1} and 0.15±0.03 mSv yr^{-1}, respectively, both exceeding the global average. The representative level index (RLI) within the study area averaged 1.96±0.32, indicating an elevated radiation risk. The excess lifetime cancer risk ($ELCR$) values for outdoor and indoor environments were 0.52×10^{-3} ±0.09 ×10^{-3} and 1.87 ×10^{-3} ±0.31×10^{-3}, respectively, surpassing the world average. Additionally, external hazard indices (H_{ex}) ranged from 0.36 to 0.59, while internal hazard indices (H_{in}) ranged from 0.38 to 1.20, both indicating values higher than UNSCEAR recommendations. These findings underscore the necessity for further experimental analysis employing ex-situ equipment. The data generated in this study can provide a valuable baseline for future assessments and interventions in radiation risk management guidelines within the country.

---

* Corresponding author at: Central Department of Physics, Tribhuvan University, Kirtipur, Kathmandu, Nepal.
E-mail address: devendra.upadhyay@ac.tu.edu.np (D.R. Upadhyay).

1. Introduction

Radiation exposure, stemming from both cosmic and primordial radionuclides in the Earth's crust, is an unavoidable facet of life. The natural presence of uranium (^{238}U), potassium (^{40}K), and thorium (^{232}Th) in the Earth's crust constitutes a significant source of natural radiation, presenting both beneficial and detrimental effects on human health. Understanding natural radioactivity is crucial for unraveling the geophysical and geochemical processes that have shaped the Earth's evolution [1]. When the Coulomb repulsive force between protons exceeds the attractive nuclear force between nucleons, nucleons become unstable, leading to disintegration through the emission of α-particles, β-particles, and γ-rays, collectively known as radiation. The impact of radiation on living organisms varies, encompassing both positive and negative effects contingent on factors such as the type of radiation, dosage, and duration of exposure. According to the International Atomic Energy Agency (IAEA), radiation effects on human health range from mild skin redness to the potential development of cancer and even death, depending on exposure levels and duration [2]. The United States Nuclear Regulatory Commission (NRC) underscores that high radiation exposure can result in cellular and tissue damage, leading to radiation sickness, cancer, and other adverse health effects [3,4]. While numerous studies have explored natural radioactivity and its hazards, only a limited number have been conducted within Nepal. Some notable works include those by [5–8], authors presented ex-situ and in-situ investigation of radiological concentrations on soils, rocks, and the environment using gamma-ray spectrometer techniques with the help of several detectors. Additionally, research has been conducted in high-background radiation areas worldwide, such as Ramsar (Iran) [9], Guarapari (Brazil) [10], Orissa and Kerala (India) [11,12], and Yangjiang (China) [13], where citizens have been living within prohibited zones [14]. These studies, like those by [9,15–18], and [19], have delved into various aspects of radiation effects, including environmental health impacts, vegetation, agriculture, and water quality [20]. This study aims to assess the health risks associated with natural radioactivity in Tarakeshwor Municipality, Kathmandu, and its surrounding areas. The presence of both natural and anthropogenic radionuclides in the environment is emerging as a significant public health concern, particularly in rapid urbanized and densely populated regions. Despite the potential risks linked to radioactivity, limited data are available regarding the levels and sources of radionuclides in the area. Therefore, the objective of in-situ study is to investigate the presence and distribution of radionuclides in the region and evaluate the potential health risks posed to the local population.

2. Materials and methods

2.1. Study area

Tarakeshwor Municipality (TM) is situated in the Kathmandu district, the capital city of Nepal, with geographical coordinates at latitude 27.7867° N and longitude: 85.3032° E, approximately. Positioned at an altitude of 1400 meters, this region is characterized by high population density, reaching 2,757 individuals per square kilometer. Historically, both Kathmandu and the Tarakeshwor Municipality were renowned for their fertile land; however, ongoing urbanization and construction activities, driven by personal, administrative and developmental purposes, have transformed the landscape [21]. TM also connected with Shivapuri Nagarjun National Park. Another fact to behind choosing this area is the seismic event of April 25, 2015, marked by a moment magnitude of 7.80, resulted in a devastating loss of approximately 8,800 lives, with thousands sustaining injuries. The earthquake also left more than 600,000 buildings in Kathmandu and the surrounding areas either damaged or completely destroyed, as documented by [22]. Notably, a report from the Department of Mines and Geology identified elevated levels of potassium concentration in the Shivapuri National Park and Panchmane area, partially encompassing TM. This revelation, previously unexplored in the context of Tarakeshwor, served as a catalyst for our investigation. Fig. 1 represents the GIS map of the study area at the ward level, complemented by maps of Kathmandu at the local level and Nepal at the district level. The seismic history, ongoing urban development, and the unique geological features prompted the selection of TM as the focal point for our study on natural radionuclide distribution and associated health risks. In the map of TM every dot represents survey location at which we did in-situ measurement of radionuclei.

2.2. Instrumentation

To collect data we used portable gamma ray information system (PGIS) which consist Scintillator detector with Sodium Iodide (Tl) - NaI(Tl) crystal. The energy resolution of NaI(Tl) 3"×3" Scintillator detector has 7.5% (at 662 keV). It is has gain stabilization automatic which is real time stabilization within 1 sec. So there is no need of calibration regularly. Also it is auto calibrated using natural background radiation, multi-peaks algorithm by statistic presence. No radioactive sources required. The measured activity concentrations of natural radionuclides using in-situ NaI(Tl) γ-ray spectrometry are estimated through evaluation of the naturally occurring terrestrial gamma radiation of ^{40}K (1461 keV) and the decay series of ^{232}Th (at 2615 keV of ^{208}Tl) and ^{238}U (at 1765 keV of ^{214}Bi) [23,24]. Fig. 2 (a) represents the gamma ray energy versus channel calibration graph shows strong positive linear correlation between these two parameters with r-value 0.99. As mentioned in International Atomic Energy Agency (IAEA) Technical Report Series No. 309 [23] and technical guidelines (IAEA-TECDOC-1363) [25] the in-situ NaI(Tl) γ-ray spectrometer is calibrated by means of calibration pads. A calibration pad is a slab of concrete containing known concentrations of the radionuclides. Another calibration method is comparing the potassium, uranium, and thorium window count rates over a calibration site with the ground concentrations of ^{238}U, ^{232}Th, and ^{40}K measured with a calibrated portable γ-ray spectrometer [23,24]. PGIS 2 operating on battery power, this device is designed to be paired with a cell phone, integrating seamlessly with an inbuilt system that facilitates coherent operation with the PGIS 2 as shown in Fig. 2 (b) and (c). All instructions and commands are inputted through the display of the
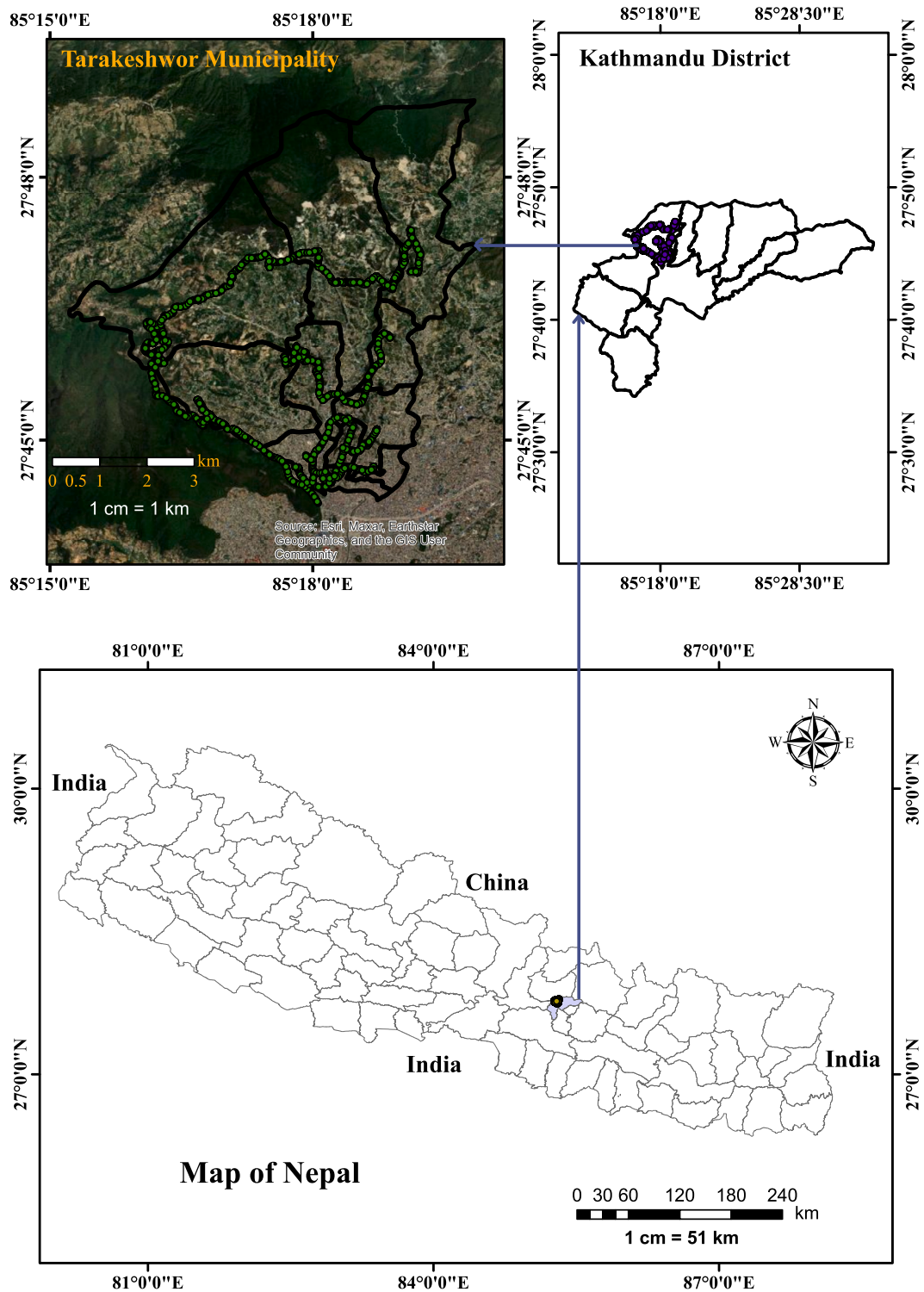
Fig. 1. Map representing surveyed area of Tarakeshwor Municipality, along with maps of Nepal and Kathmandu district.

Fig. 2. (a) Energy calibration graph shows relation between energy and channel number. (b) At study area with Portable Gamma spectrometer Information System (PGIS 2) having specifications: NaI(Tl) crystal: 3"×3" (0.347 L), 512 channel spectrometer, energy range 20 keV - 3 MeV. (c) Mobile set connected via Bluetooth to the detector.

connected cell phone. During measurements, the device was placed positioned 1 meter above the ground, secured inside a backpack or handheld, and oriented towards the sky. Gamma ray spectrometry as shown in Fig. 2 (b) and (c) a non-destructive analytical method, was utilized to identify and quantify radioactive isotopes present in environment by measuring emitted gamma rays. When gamma rays strike the detector, they generate light or electrical charges, which are then detected and converted into an electrical signal. The resulting spectrum is a graphical representation of the number of detected gamma rays as a function of their energy. We measure the concentrations of ^{238}U, ^{232}Th and ^{40}K in terms of parts per million (ppm) and percentage (%). Using conversion factors provided in IAEA Technical Report Series No. 309 and Technical Guidelines (IAEA-TECDOC-1363) [25]. Specifically, for ^{238}U, 1 ppm is equivalent to 12.35 Bq kg^{-1}, for ^{232}Th, 1 ppm equals 4.06 Bq kg^{-1}, and for ^{40}K, 1% corresponds to 313 Bq kg^{-1} [23,25] as shown in Table 1.

For data analysis and processing, several software tools were employed. PEIView software used for data extraction, ArcGIS, a robust GIS software developed by Esri, played a pivotal role to visualize data. Widely used by professionals and organizations, ArcGIS aids in the analysis of complex spatial problems and the extraction of insights from geographic data. In this study, ArcGIS facilitated various tasks, including the conversion of problems into research questions, the creation of a geographic database, data analysis, and interpretation of results. Python-3, the latest major version of the Python programming language, was utilized for diverse purposes such as data analysis, visualization, and scientific computing. The hazards indices calculations, bar diagrams, best fit plots, and error analysis were performed using Python-3. Excel was employed for tabulation, data reduction, and organization of data in this work, contributing to an efficient workflow for managing and interpreting research data. The combined use of these tools ensured a comprehensive and accurate analysis of the gathered information, enhancing the robustness of the presented study.

2.3. Theoretical background

Calculation of Hazard Indices

The radiological parameters were determined using the empirical formula reported by [26], a methodology widely adopted [26–28] as shown in Table 1. It shows 14 parameters of radiological quantity, their units, formulae, corresponding safe limit of each parameters and references.

Here, D_R represents the gamma absorbed dose rate (GADR) with occupancy factors of 0.8 and 0.2, a conversion coefficient of 0.7, and a time span of 8760 hours per year (equivalent to 365 days) [31,37–39].

The activity concentrations of ^{238}U, ^{232}Th, and ^{40}K, denoted as A_U, A_{Th}, and A_K respectively, are measured in units of Bq kg^{-1}. The fractional contributions to the total dose rate resulting from radiation emitted by ^{238}U, ^{232}Th, and ^{40}K are represented as f_U (0.46), f_{Th} (0.60), and f_K (0.04) respectively. Factors DL and RF correspond to the duration of average life (70 years) of people and risk factor (Sv^{-1}), which indicates the fatal cancer risk per Sievert. ICRP 60 guidelines consider a value of 0.05 for the public when addressing stochastic effects [26,37–40]. These parameters collectively contribute to the calculation of hazard indices, providing insights into the potential health risks associated with the observed natural radioactivity in the study area. All formula used for the calculation of equivalent activity, dose rates (per hour and per year), associated hazard indices are presented in Table 1.

2.4. Statistical analysis

The obtained results were subjected to comprehensive statistical analysis using Libre Office Calculator and Python 3. Pearson correlation coefficients were computed to scrutinize relationships between variables following methodologies applied by Ravisankar et al. (2014) [33] and Tchorz-Trzeciakiewicz, Kozłowska, & Walencik-Łata (2023) [41]. Additionally, various statistical measures were employed to characterize the data distribution and central tendencies. These measures include mean, standard deviation (σ), minimum (Min), maximum (Max), quartiles (Q_1, Q_2, and Q_3), range, skewness, kurtosis, variance, median absolute deviation (MAD),

Table 1
Hazard indices.

S.N.	Radiological Quantity	Units	Formula	Safe Limit	References
1	Activity	Bq kg^{-1}	For ^{238}U, 1 ppm = 12.35 Bq kg^{-1}, ^{232}Th, 1 ppm = 4.06 Bq kg^{-1} and ^{40}K, 1% = 313 Bq kg^{-1}	$\leq$ 33 for ^{238}U, 45 for ^{232}Th 420 and for ^{40}K	[16,23–25]
2	Radium equivalent index	Bq kg^{-1}	$Ra_{eq} = A_U + 1.43A_{Th} + 0.077A_K$	$\leq$ 370	[16,26]
3	Absorbed dose rate	nSv hr^{-1}	$D_R = 0.427A_U + 0.662A_{Th} + 0.0432A_K$	$\leq$ 59	[28–30]
4	Indoor annual effective dose equivalent	mSv yr^{-1}	$AEDE_{outdoor} = D_R(\text{nSvhr}^{-1}) \times 8760\,(\text{hr}) \times 0.7(\text{Sv Gy}^{-1}) \times 0.7 \times 10^{-6}$	$\leq$ 0.48	[26,31]
5	Outdoor annual effective dose equivalent	mSv yr^{-1}	$AEDE_{outdoor} = D_R(\text{nGy hr}^{-1}) \times 8760\,(\text{hr}) \times 0.7(\text{Sv Gy}^{-1}) \times 0.2 \times 10^{-6}$	$\leq$ 0.48	[26,31]
6	Indoor excess lifetime cancer risk		$ELCR_{indoor} = AEDE_{indoor} \times DL \times RF$	$\leq$ 0.29	[32,33]
7	Outdoor excess lifetime cancer risk		$ELCR_{outdoor} = AEDE_{outdoor} \times DL \times RF$	$\leq$ 0.29	[32,33]
8	Annual gonadal dose equivalent	μSv yr^{-1}	$AGDE = 3.09A_U + 4.18A_{Th} + 0.214A_K$	$\leq$ 300	[32,33]
9	Internal hazard index	-	$H_{in} = \frac{A_U}{185} + \frac{A_{Th}}{259} + \frac{A_K}{4810}$	$\leq$ 1	[16,26]
10	External hazard index	-	$H_{ex} = \frac{A_U}{370} + \frac{A_{Th}}{259} + \frac{A_K}{4810}$	$\leq$ 1	[16,26]
11	Gamma index	-	$I_\gamma = \frac{A_U}{300\ \text{Bq kg}^{-1}} + \frac{A_{Th}}{200\ \text{Bq kg}^{-1}} + \frac{A_K}{3000\ \text{Bq kg}^{-1}}$	$\leq$ 6	[26,33]
12	Alpha index	-	$I_\alpha = \frac{A_U}{200}$	$\leq$ 1	[34,35]
13	Representative level index	-	$RLI = \frac{A_U}{150} + \frac{A_{Th}}{100} + \frac{A_K}{1500}$	$\leq$ 1	[34,35]
14	Activity utilization index	-	$AUI = \left(\frac{A_U}{50\ \text{Bq kg}^{-1}}\right)f_U + \left(\frac{A_{Th}}{50\ \text{Bq kg}^{-1}}\right)f_{Th} + \left(\frac{A_K}{500\ \text{Bq kg}^{-1}}\right)f_K$	$\leq$ 2	[32,36]

and coefficient of variation (CV). Python programming facilitated the computation and analysis of these statistical parameters following the methodologies outlined by Ghias et al. (2021) [42] and Ravisankar et al. (2014) [33]. The statistical analysis using Univariate (bar diagram), Bivariate (regression analysis) and Multivariate (spatial distribution) analysis using Python 3 and ArcMap provides a comprehensive understanding of the distributional characteristics, variability, and relationships within the data set, contributing valuable insights to the interpretation of the research findings.

3. Results and discussion

The results of the presented work are presented in the form of bar diagram with error bars, best fitted lines, distribution maps using ArcMap 10.8, and statistical analysis. Fig. 3 show the activity concentration of radio nucleides at specific location such as at health post (HP), ward office (WO), school (SC), construction areas (CA), very close ward office and health post are denoted by WOHP and TM6 represents the premises of Tarakeshwor Municipality which lies in ward 6. Sometime we found ward office and health post close to each other so we have presented only one place survey by combining both region. Here bar diagram represents the concentration of radionuclide: ^{238}U (red bar), ^{232}Th (blue) and ^{40}K (black bar) and error bar represents the standard error of data at every locations. Additionally we compared those obtained data with UNSCEAR [26] recommended limit for environmental radioactivity. We obtained most of the region has those values above the world average values.

Table 2 and Table 3 represents radionuclide concentration and associated hazard indices measured and estimated parameters at public places of different wards of TM. Here, radionuclide concentration of uranium (^{238}U), thorium (^{232}Th), and potassium (^{40}K) are presented in Bq kg^{-1} along with standard error. Radium equivalent abbreviated as (Ra_{eq}) is expressed in Bq kg^{-1}. Dose rate (D_R) is expressed in nSv hr^{-1}. Similarly, annual effective dose rate for outdoor and indoor ($AEDR_O$ and $AEDR_I$) and annual gonadal dose equivalent ($AGDE$) expressed in mSv yr^{-1} are presented in Table 2. Similarly, $ELCR_O$, $ELCR_I$, H_{in}, H_{ex}, I_G, AI, RLI, and AUI are tabulated as shown in Table 3. Here, HP indicates health post, WO indicates ward office, SC represents school CA represents construction area, WOHP represents ward office and health post located at the same site, TM represents municipality office, and SIH denotes Shivam International Hospital. And the numeric value after the alphabet represents the respective ward numbers. For instance, CA1 means construction area of ward No.1 of Tarakeshwor Municipality. Fig. 4 (a) demonstrates a best fit of Ra_{eq} and ^{238}U concentration. Pearson correlation coefficient was found to be 0.82, which stated lucidly that there is a strong correlation between Ra_{eq} and ^{238}U concentration. The best fitted line we obtained is given by Eq. (1).

$$Ra_{eq} = 2.37\ ^{238}\text{U} + 77.08 \qquad\qquad (1)$$

where, 2.37 and 77.08 are the values of slope and intercept respectively as shown in Fig. 4 (a). Fig. 4 (b) demonstrates a best fit of Ra_{eq} and ^{232}Th concentration. Pearson correlation coefficient was found to be 0.95, which stated precisely that there is a strong correlation between Ra_{eq} and ^{232}Th concentration. The best fitted line we obtained is given by Eq. (2).

$$Ra_{eq} = 2.30\ ^{232}\text{Th} + 82.87 \qquad\qquad (2)$$
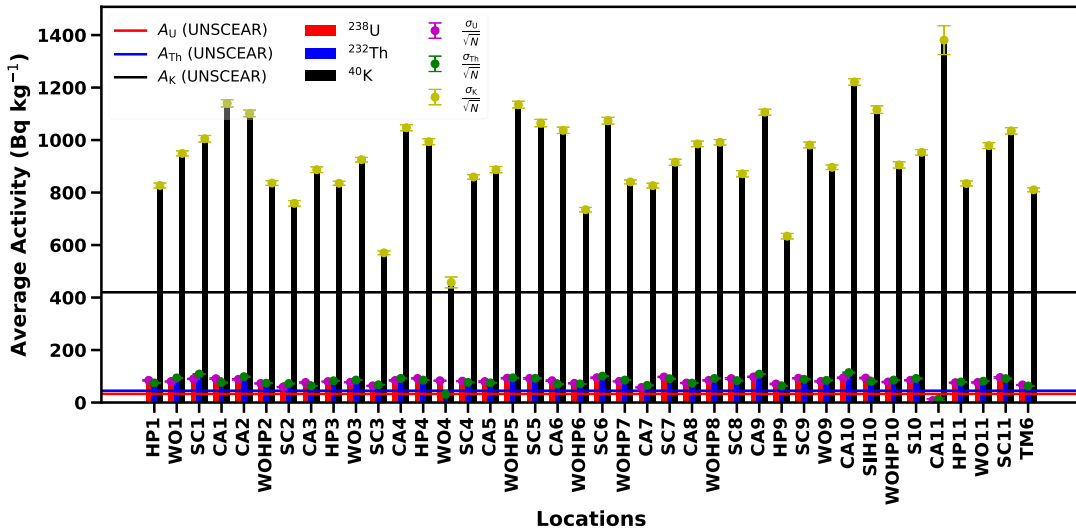
Fig. 3. Summary of concentration of naturally occurring radioactive nuclei: ^{238}U, ^{232}Th and ^{40}K. Bars represent the measured value of radionuclei. The error bar represents the standard error ($\frac{\sigma}{\sqrt{N}}$) and horizontal lines indicated UNSCEAR [26] recommended values in the environment.
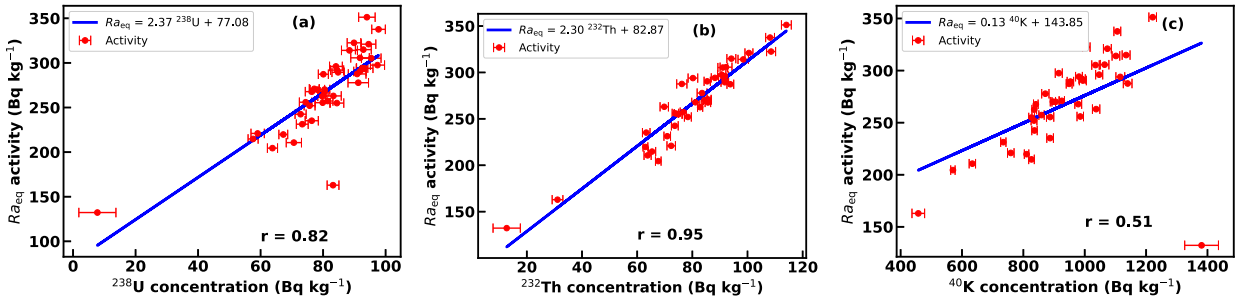

Fig. 4. Correlation between activity concentration of ^{238}U, ^{232}Th, ^{40}K and radium equivalent.

where, 2.30 and 82.87 are the values of slope and intercept, respectively as shown in Fig. 4 (b). Fig. 4 (c) demonstrates a best fit of Ra_{eq} and ^{40}K concentration. Pearson correlation coefficient was found to be 0.51, which stated distinctly that there is a moderate correlation between Ra_{eq} and ^{40}K concentration. The best fitted line we obtained is given by Eq. (3).

$$Ra_{eq} = 0.13\ ^{40}K + 143.85 \tag{3}$$

where, 0.13 and 143.85 are the values of slope and intercept, respectively as shown in Fig. 4 (c). It can be stated from observing plots that, the more r value close to 1, the more points lies along the lines. Similarly, as the r value goes on decreasing, the points are dispersing/ diverging from the lines. Fig. 5 (a) represents the topographical mapping of the survey area TM presented along with the co-ordinates. Here, the activity concentration of uranium ^{238}U is plotted and expressed in Bq kg^{-1}. Here, black rectangles indicates the activity concentration from 7.78 to 33.00 Bq kg^{-1}, which is the world average value for uranium ^{238}U. Similarly, blue stars, red triangles, and radiation symbols denotes the activity concentration from 33.00 to 70.64 Bq kg^{-1}, 70.65 to 84.79 Bq kg^{-1}, and 84.80 to 97.75 Bq kg^{-1} respectively. It can be inferred that all the surveyed location have greater activity concentration of uranium (^{238}U) than world average value. In figure, it is seem that red triangles and radiation symbols dominates others, which means most of the location have activity concentration of uranium ^{238}U between 70.65 to 97.75 Bq kg^{-1}, which is greater than world average value. Fig. 5 (b) shows the topographical mapping plotted with the activity concentration of thorium ^{232}Th, expressed in Bq kg^{-1}. Here, black rectangles indicates the activity concentration from 12.70 to 45.00 Bq kg^{-1}, which is the world average value for thorium ^{232}Th. Similarly, blue stars, red triangles, and radiation symbols denotes the activity concentration from 45.00 to 78.38 Bq kg^{-1}, 78.38 to 94.14 Bq kg^{-1}, and 94.14 to 114.09 Bq kg^{-1} respectively. It can be inferred from the figure that most of the surveyed location have greater activity concentration due to thorium ^{232}Th than world average value. In figure, it is seem that blue stars and red triangles dominates others, which means most of the location have activity concentration of thorium ^{232}Th between 45.00 to 94.14 Bq kg^{-1}. Fig. 5 (c) represents the topographical mapping plotted with the activity concentration of potassium ^{40}K, expressed in Bq kg^{-1}. Here, black rectangles indicates the activity concentration from 457.59 to 840.00 Bq kg^{-1}, which is twice the world average value for potassium ^{40}K. Similarly, blue stars, red triangles, and radiation symbols denotes the activity concentration from 840.00 to 925.26 Bq kg^{-1}, 925.26 to 1073.78 Bq kg^{-1}, and 1073.78 to 1380.80 Bq kg^{-1} respectively. It shows that all of the

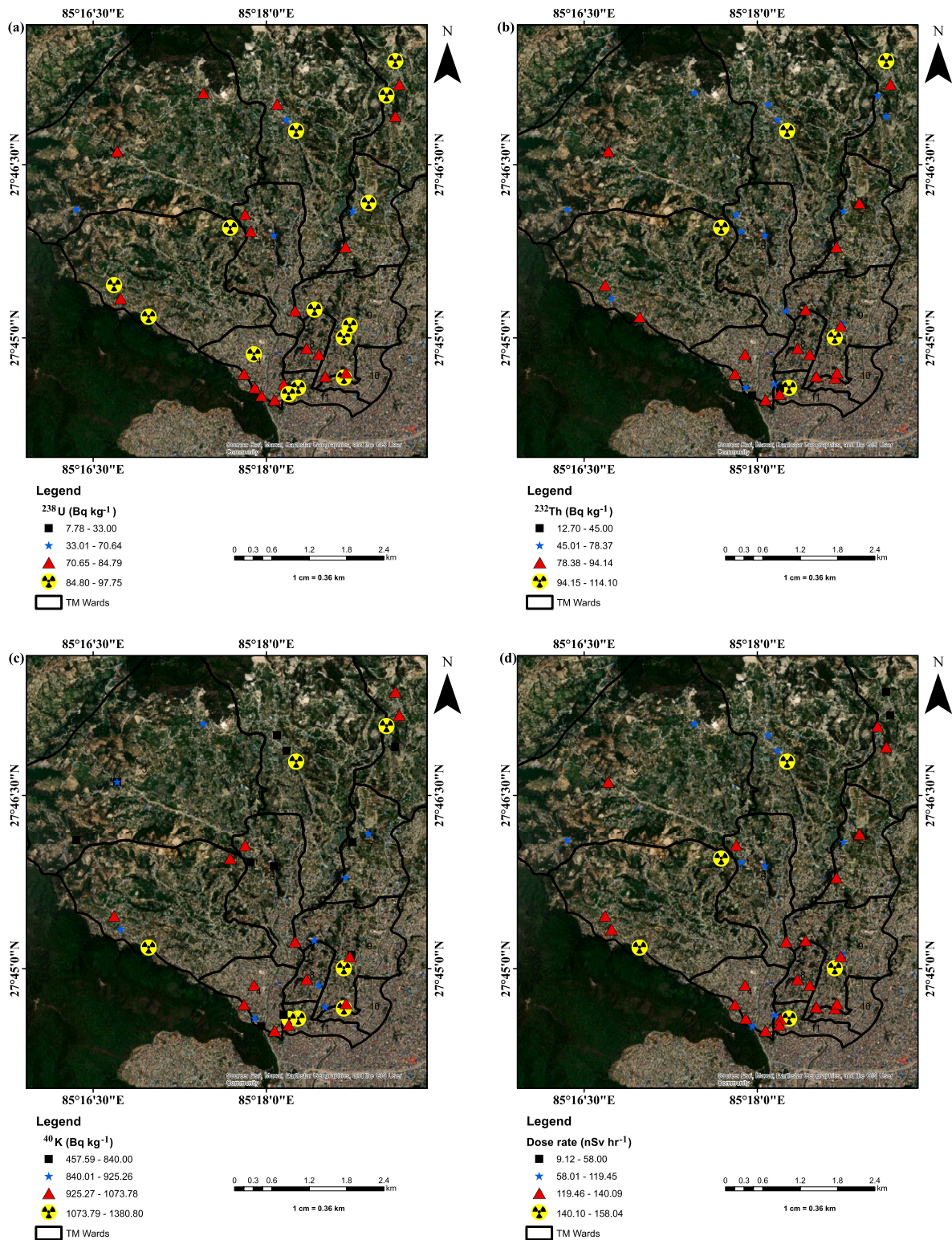**Fig. 5.** Distribution of activity concentration of (a) ^{238}U, (b) ^{232}Th, (c) ^{40}K and (d) Gamma dose rate (nSv hr^{-1}) mapping of study region with base map at four public places from each wards of Tarakeshowar Municipality, Kathmandu.

Table 2
Radionuclei concentration and associated hazard indices: R_{eq}, D_R, $AEDR_O$, $AEDR_I$.

Public Places	$^{238}U \pm \sigma_U$ (Bq kg^{-1})	$^{232}Th \pm \sigma_{Th}$ (Bq kg^{-1})	$^{40}K \pm \sigma_K$ (Bq kg^{-1})	R_{eq} (Bq kg^{-1})	D_R (nSv hr^{-1})	$AEDR_O$ (mSv yr^{-1})	$AEDR_I$ (mSv yr^{-1})
HP1	84.41 ± 36.68	74.74 ± 24.94	826.89 ± 155.07	254.96	118.17	0.14	0.51
WO1	80.08 ± 40.39	93.78 ± 30.84	949.21 ± 239.05	287.27	133.39	0.16	0.57
SC1	89.89 ± 37.19	108.55 ± 27.81	1005.14 ± 209.33	322.52	149.20	0.18	0.64
CA1	90.90 ± 38.60	76.19 ± 25.28	1139.88 ± 192.94	287.61	135.22	0.17	0.58
CA2	88.43 ± 39.02	98.45 ± 28.89	1101.64 ± 191.47	314.04	146.40	0.18	0.63
WOHP2	72.80 ± 34.17	73.64 ± 23.78	836.26 ± 170.26	242.51	112.89	0.14	0.48
SC2	59.06 ± 29.70	72.34 ± 21.32	759.00 ± 148.55	220.95	102.87	0.13	0.44
CA3	76.37 ± 30.24	63.29 ± 19.75	887.11 ± 155.41	235.18	110.15	0.14	0.47
HP3	79.78 ± 37.22	82.82 ± 23.94	835.46 ± 191.26	262.53	121.57	0.15	0.52
WO3	77.18 ± 34.34	85.68 ± 24.58	925.26 ± 186.99	270.94	126.07	0.15	0.54
SC3	63.80 ± 31.48	67.65 ± 19.74	570.40 ± 138.42	204.46	93.94	0.12	0.40
CA4	84.11 ± 36.60	91.84 ± 21.58	1047.06 ± 206.31	296.06	138.09	0.17	0.59
HP4	91.79 ± 36.87	85.40 ± 21.06	993.80 ± 211.15	290.44	135.11	0.17	0.58
WO4	83.18 ± 34.21	31.12 ± 35.21	457.59 ± 372.91	162.92	74.70	0.09	0.32
SC4	81.45 ± 34.88	76.70 ± 22.57	859.19 ± 177.15	257.28	119.49	0.15	0.51
CA5	79.88 ± 36.75	74.99 ± 22.17	887.20 ± 181.69	255.43	118.95	0.15	0.51
WOHP5	92.87 ± 38.67	94.14 ± 24.61	1134.84 ± 196.12	314.88	147.04	0.18	0.63
SC5	91.82 ± 39.33	92.22 ± 28.60	1064.74 ± 185.44	305.67	142.40	0.17	0.61
CA6	83.30 ± 37.25	69.81 ± 22.42	1037.13 ± 178.17	262.99	123.60	0.15	0.53
WOHP6	73.33 ± 33.98	70.90 ± 21.43	734.65 ± 154.64	231.29	107.07	0.13	0.46
SC6	94.57 ± 43.39	100.52 ± 27.17	1073.78 ± 241.56	320.99	149.14	0.18	0.64
WOHP7	80.46 ± 32.60	85.63 ± 23.27	840.58 ± 173.69	267.63	123.84	0.15	0.53
CA7	57.61 ± 27.73	65.39 ± 22.62	826.47 ± 157.56	214.76	100.80	0.12	0.43
SC7	97.41 ± 35.04	90.65 ± 23.26	915.42 ± 177.32	297.53	137.45	0.17	0.59
CA8	74.41 ± 35.39	73.87 ± 20.86	985.40 ± 187.19	255.67	120.09	0.15	0.52
WOHP8	84.48 ± 36.67	91.69 ± 21.71	991.54 ± 178.71	291.94	135.79	0.17	0.58
SC8	91.25 ± 48.40	83.52 ± 26.19	871.60 ± 174.90	277.80	128.49	0.16	0.55
CA9	97.74 ± 43.40	108.18 ± 31.98	1106.16 ± 223.51	337.62	156.66	0.19	0.67
HP9	70.64 ± 36.08	63.78 ± 19.09	633.76 ± 153.96	210.65	97.17	0.12	0.42
SC9	92.51 ± 38.24	88.19 ± 28.23	981.20 ± 235.38	294.18	136.62	0.17	0.59
WO9	80.47 ± 36.94	84.38 ± 25.24	896.24 ± 186.91	270.14	125.44	0.15	0.54
CA10	94.02 ± 43.08	114.09 ± 29.16	1221.42 ± 202.45	351.22	163.66	0.20	0.70
SIH10	93.29 ± 35.84	80.21 ± 23.43	1115.92 ± 193.40	293.92	137.74	0.17	0.59
WOHP10	78.17 ± 38.89	85.43 ± 23.41	905.29 ± 202.71	270.04	125.49	0.15	0.54
S10	84.79 ± 36.87	91.77 ± 25.85	953.24 ± 198.65	289.43	134.34	0.16	0.58
CA11	7.78 ± 94.70	12.70 ± 79.02	1380.80 ± 878.11	132.26	70.22	0.09	0.30
HP11	75.68 ± 29.82	78.38 ± 21.36	834.65 ± 161.15	252.03	117.01	0.14	0.50
WO11	76.42 ± 33.01	81.12 ± 20.81	978.79 ± 173.57	267.79	125.20	0.15	0.54
SC11	95.41 ± 43.96	91.03 ± 24.87	1035.05 ± 171.20	305.29	141.94	0.17	0.61
TM6	67.27 ± 31.82	63.00 ± 19.67	810.45 ± 164.44	219.76	102.78	0.13	0.44
[26]	33	45	420	370	59	0.07	0.26
Mean	80.47	80.44	935.26	267.52	124.65	0.15	0.54
σ	15.52	18.58	172.30	44.79	20.29	0.03	0.09
Min	7.78	12.70	457.59	132.26	70.22	0.09	0.30
Q_1	76.20	73.32	836.06	249.65	115.98	0.14	0.50
Median	82.32	83.17	937.23	270.09	125.46	0.15	0.54
Q_3	91.30	91.71	1039.62	294.65	137.52	0.17	0.59
Max	97.74	114.09	1380.80	351.22	163.66	0.20	0.70
Range	89.96	101.40	923.21	218.96	93.45	0.12	0.40
Skewness	-2.66	-1.40	-0.28	-0.81	-0.66	-0.66	-0.66
Kurtosis	10.11	3.68	1.02	0.99	0.46	0.46	0.46
Variance	241.04	345.28	29687.74	2006.05	411.73	1.00×10^{-3}	0.01
MAD	9.89	12.97	129.58	33.60	15.42	0.02	0.07
CV	19.29	23.10	18.42	16.74	16.28	16.28	16.28

surveyed location have greater activity concentration due to potassium ^{40}K than world average value. It is inferred that this area have prolific amount of activity concentration due to potassium ^{40}K. Fig. 5 (d) presents the spatial mapping with dose rate, expressed in nSv hr^{-1}. Here, black rectangles indicates the dose rate from 102.92 to 114.00 nSv hr^{-1}. Similarly, blue stars, red triangles, and radiation symbols denotes the dose rate from 114.00 to 129.89 nSv hr^{-1}, 129.89 to 140.09 nSv hr^{-1}, and 140.09 to 158.03 nSv hr^{-1}, respectively. The graphs presented in the Fig. 6 represents the best fit of activity concentration due to ^{238}U, ^{232}Th, and ^{40}K with dose rate. Here, blue lines are the best fit lines and red dots are the coordinates indicating dose rate and activity concentration, horizontal axis represents activity concentrations expressed in Bq kg^{-1}, and along vertical axis presented find the dose rate expressed in nSv hr^{-1}. Each bivariate plots is presented with the Pearson correlation coefficient (i.e. r value), slope, and intercept. Fig. 6 (a) demonstrates a best fit of D_R and ^{238}U concentration. Pearson correlation coefficient was found to be 0.79, which stated distinctly that there is a strong correlation between D_R and ^{238}U concentration. The best fitted line we obtained is given by Eq. (4).

Table 3
Locations and associated hazard indices: $ELCR_o$, $ELCR_I$, $AGDE$, H_{in}, H_{ex}, I_γ, I_α, RLI, and AUI.

Public Places	$ELCR_O$ $\times 10^{-3}$	$ELCR_I$ $\times 10^{-3}$	$AGDE$ (μSv yr^{-1})	H_{in}	H_{ex}	I_γ	I_α	RLI	AUI
HP1	0.51	1.78	750.19	0.92	0.69	0.93	0.42	1.86	1.75
WO1	0.57	2.00	842.58	0.99	0.78	1.05	0.40	2.10	1.95
SC1	0.64	2.24	946.61	1.11	0.87	1.18	0.45	2.35	2.23
CA1	0.58	2.03	843.26	1.02	0.78	1.06	0.45	2.13	1.86
CA2	0.63	2.20	920.52	1.09	0.85	1.15	0.44	2.31	2.10
WOHP2	0.48	1.70	711.75	0.85	0.65	0.89	0.36	1.78	1.63
SC2	0.44	1.55	647.29	0.76	0.60	0.81	0.30	1.62	1.48
CA3	0.47	1.65	690.37	0.84	0.64	0.87	0.38	1.73	1.54
HP3	0.52	1.83	771.47	0.92	0.71	0.96	0.40	1.92	1.81
WO3	0.54	1.89	794.61	0.94	0.73	0.99	0.39	1.99	1.83
SC3	0.40	1.41	602.00	0.72	0.55	0.74	0.32	1.48	1.45
CA4	0.59	2.07	867.86	1.03	0.80	1.09	0.42	2.18	1.97
HP4	0.58	2.03	853.28	1.03	0.78	1.06	0.46	2.13	1.96
WO4	0.32	1.12	485.05	0.66	0.44	0.59	0.42	1.17	1.18
SC4	0.51	1.80	756.13	0.92	0.69	0.94	0.41	1.88	1.75
CA5	0.51	1.79	750.14	0.91	0.69	0.94	0.40	1.87	1.72
WOHP5	0.63	2.21	923.35	1.10	0.85	1.16	0.46	2.32	2.09
SC5	0.61	2.14	897.04	1.07	0.83	1.12	0.46	2.24	2.05
CA6	0.53	1.86	771.16	0.94	0.71	0.97	0.42	1.94	1.70
WOHP6	0.46	1.61	680.18	0.82	0.62	0.84	0.37	1.69	1.60
SC6	0.64	2.24	942.17	1.12	0.87	1.18	0.47	2.35	2.18
WOHP7	0.53	1.86	786.43	0.94	0.72	0.98	0.40	1.95	1.85
CA7	0.43	1.51	628.21	0.74	0.58	0.79	0.29	1.59	1.39
SC7	0.59	2.06	875.82	1.07	0.80	1.08	0.49	2.17	2.07
CA8	0.52	1.80	749.56	0.89	0.69	0.95	0.37	1.89	1.66
WOHP8	0.58	2.04	856.49	1.02	0.79	1.07	0.42	2.14	1.97
SC8	0.55	1.93	817.62	1.00	0.75	1.01	0.46	2.02	1.92
CA9	0.67	2.35	990.94	1.18	0.91	1.24	0.49	2.47	2.30
HP9	0.42	1.46	620.51	0.76	0.57	0.77	0.35	1.53	1.48
SC9	0.59	2.05	864.48	1.04	0.79	1.08	0.46	2.15	2.00
WO9	0.54	1.88	793.13	0.95	0.73	0.99	0.40	1.98	1.84
CA10	0.70	2.46	1028.81	1.20	0.95	1.29	0.47	2.58	2.35
SIH10	0.59	2.07	862.35	1.05	0.79	1.08	0.47	2.17	1.92
WOHP10	0.54	1.89	792.37	0.94	0.73	0.99	0.39	1.98	1.83
S10	0.58	2.02	849.62	1.01	0.78	1.06	0.42	2.12	1.97
CA11	0.30	1.05	372.61	0.38	0.36	0.55	0.04	1.10	0.34
HP11	0.50	1.76	740.08	0.89	0.68	0.92	0.38	1.84	1.72
WO11	0.54	1.88	784.70	0.93	0.72	0.99	0.38	1.97	1.77
SC11	0.61	2.13	896.84	1.08	0.82	1.12	0.48	2.24	2.07
TM6	0.44	1.54	644.62	0.78	0.59	0.81	0.34	1.62	1.45
[26]	0.26	0.90	300	1	1	1	1	1	2
Mean	0.54	1.87	785.06	0.94	0.72	0.98	0.40	1.96	1.79
σ	0.09	0.31	132.11	0.16	0.12	0.16	0.08	0.32	0.35
Min	0.30	1.06	372.61	0.38	0.36	0.55	0.04	1.10	0.34
Q_1	0.50	1.74	731.00	0.88	0.67	0.91	0.38	1.83	1.66
Median	0.54	1.89	792.75	0.94	0.73	0.99	0.41	1.98	1.83
Q_2	0.59	2.07	865.33	1.05	0.80	1.08	0.46	2.17	1.98
Max	0.70	2.46	1028.81	1.20	0.95	1.29	0.49	2.58	2.35
Range	0.40	1.40	656.20	0.82	0.59	0.74	0.45	1.48	2.01
Skewness	-0.66	-0.66	-0.86	-1.16	-0.81	-0.67	-2.66	-0.67	-1.77
Kurtosis	0.46	0.46	1.18	2.38	0.99	0.50	10.11	0.50	5.61
Variance	0.01	0.09	17452.57	0.03	0.02	0.03	0.01	0.10	0.12
MAD	0.07	0.23	98.75	0.12	0.09	0.12	0.05	0.24	0.24
CV	16.28	16.28	16.83	16.73	16.74	16.34	19.29	16.34	19.53

$$D_R = 1.03 \; ^{238}U + 41.57 \tag{4}$$

where, 1.03 and 41.58 are the values of slope and intercept, respectively as shown in Fig. 6 (a). Fig. 6 (b) demonstrates a best fit of D_R and ^{232}Th concentration. Pearson correlation coefficient was found to be 0.98, which stated distinctly that there is a high degree of correlation between D_R and ^{232}Th concentration. The best fitted line we obtained is given by Eq. (5).

$$D_R = 1.02 \; ^{232}Th + 42.33 \tag{5}$$

where, 1.02 and 42.33 are the values of slope and intercept, respectively as shown in Fig. 6 (b). Fig. 6 (c) demonstrates a best fit of D_R and ^{40}K concentration. Pearson correlation coefficient was found to be 0.57, which stated precisely that there is a moderate correlation between D_R and ^{40}K concentration. The best fitted line we obtained is given by Eq. (6).

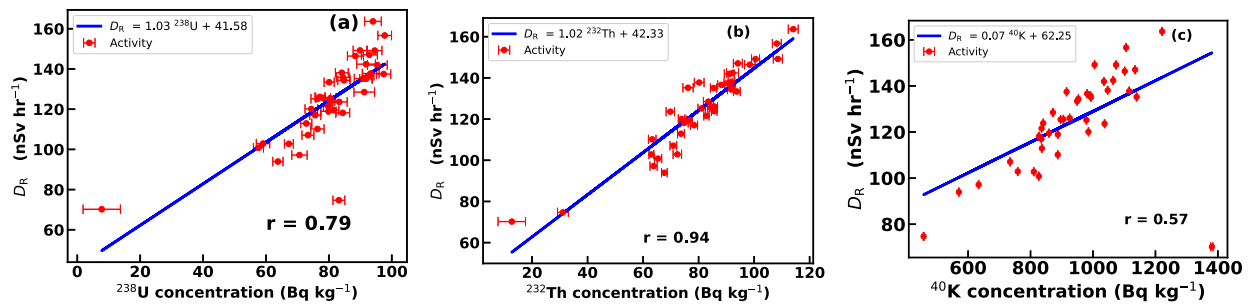**Fig. 6.** Correlation between activity concentration of ^{238}U, ^{232}Th, ^{40}K with dose rate.

Table 4
Comparison of activity concentration and hazard indices with different parts of the world.

Particulars	A_U Bq kg^{-1}	A_{Th} Bq kg^{-1}	A_K Bq kg^{-1}	R_{eq} Bq kg^{-1}	D_R nSv hr^{-1}	$AEDR_O$ mSv yr^{-1}	$AEDR_I$ mSv yr^{-1}	$ELCR_O$ ×10^{-3}	References
Poland	-	-	-		-	0.52	-	-	[41]
Nepal	108.41±29.66	102.06±28.25	1082.35±251.03		152.32±15.07	-	-	-	[8]
Nigeria	-	64.89 ± 1.50	181.38± 2.22	134.97	61.68	0.08	-	-	[45]
Nigeria	35.44 ± 0.97	92.57 ± 1.17	137.59 ± 2.42	202.15	84.77 ± 0.97	0.08	-	-	[16]
Korea	63.1 ± 1.3	99.2 ± 1.5	1060 ± 14	-		125 ± 6	-	-	[24]
Kenya	240±17	626 ±27	401±21	-	408±20	2.37±0.09	-	-	[18]
South Africa	-	64	390	-	-	0.08	-	-	[43]
Egypt	947	64	33.2	499.0 - 3484.9	149.5 - 970	0.18 - 1.19	-	0.002±0.001	[46]
Soil Iraq	13	20	215	58	28	0.03	0.14	0.13	[47]
Himalayan Soil	36	50	1595	228	112	0.55	0.14	-	[44]
India Soil	97	129	541	322	145	0.7	0.2	-	[20]
Orissa, India	350 ± 20	2825 ± 50	180 ± 25		1925 ± 40	-	-	-	[11]
KMC Soil	10.81	47.92	44.80	82.80	36.39	0.05	0.18	0.19	[5]
Present work	**80.47±15.53**	**80.44±18.58**	**935.26±172.30**	**267.52±44.79**	**124.65±20.29**	**0.15±0.03**	**0.54±0.09**	**0.54±0.09**	**TM**
UNSCEAR	33	45	420	370	59	0.07	0.26	0.26	[26]

$$D_R = 0.07\ ^{40}K + 62.25 \tag{6}$$

where, 0.07 and 62.25 are the values of slope and intercept, respectively as shown in Fig. 6 (c). Fig. 7 shows map plotted with the dynamic data collected across the survey. Nearly, 12,000 dynamic data were collected during survey. Co-ordinates also can be seen along the margin of the map. Solid black curves represents the border of the wards of TM. Fig. 7 (a) is the activity distribution plotted with the uranium (^{238}U) activity concentration, expressed in Bq kg^{-1}. Here, black rectangles indicates the range of concentration from 3.06 to 33.00 Bq kg^{-1}. Similarly, blue stars, red triangles, and radiation symbols represents range of concentration from 33.00 to 92.43 Bq kg^{-1}, 92.43 to 131.97 Bq kg^{-1}, and 131.97 to 316.83 Bq kg^{-1}, respectively. Fig. 7 (b) is the distribution plotted with the thorium (^{232}Th) activity concentration, expressed in Bq kg^{-1}. Here, black rectangles indicates the range of concentration from 2.64 to 45.00 Bq kg^{-1}. Similarly, blue stars, red triangles, and radiation symbols represents range of concentration from 45.00 to 88.32 Bq kg^{-1}, 88.32 to 116.73 Bq kg^{-1}, and 116.73 to 242.64 Bq kg^{-1}, respectively. Fig. 7 (c) is the activity distribution plotted with the potassium (^{40}K) activity concentration, expressed in Bq kg^{-1}. Here, black rectangles indicates the range of concentration from 84.82 to 420.00 Bq kg^{-1}. Similarly, blue stars, red triangles, and radiation symbols represents range of concentration from 420.00 to 920.85 Bq kg^{-1}, 920.85 to 1162.48 Bq kg^{-1}, and 1162.48 to 1811.33 Bq kg^{-1}, respectively. Fig. 7 (d) is the map plotted with the dose rate, expressed in nSv hr^{-1}. Here, black rectangles indicates the range of dose rate from 87.32 to 114.00 nSv hr^{-1}. Similarly, blue stars, red triangles, and radiation symbols represents range of dose rate from 114.00 to 128.76 nSv hr^{-1}, 128.76 to 143.50 nSv hr^{-1}, and 143.497 to 197.037 nSv hr^{-1}, respectively. The comparative study of the presented work with similar work from several regions of the world are tabulated in Table 4 and Table 5. It is distinctly seen that the activity concentrations of the present work are greater than double of world average for potassium (^{40}K) and uranium (^{238}U), and slightly less than double of world average for thorium (^{232}Th). It can be inferred from the table that activity concentration of uranium (^{238}U) is highest in Egypt [43], that is 947 Bq kg^{-1}. Similarly, among the tabulated values, activity concentrations of thorium (^{232}Th), potassium (^{40}K) and dose rate are highest in Kenya [18], and Nepal [8] respectively. Additionally we compared in-situ with ex-situ measurement of radionuclei and associated hazard at near city [5] to the present study area and high activity [11] and Himalayan region study of nearby country India [20,44]. Health hazards indices are also presented and compared in the table.

4. Conclusions

The mobile in-situ radiometric study was conducted in Tarakeshwor Municipality, encompassing all 11 wards of the region significantly affected by the Nepal earthquake in 2015. Utilizing a portable gamma-ray spectrometer, the survey collected static data from various locations, including construction areas, schools, ward offices, and health posts, alongside dynamic data collected
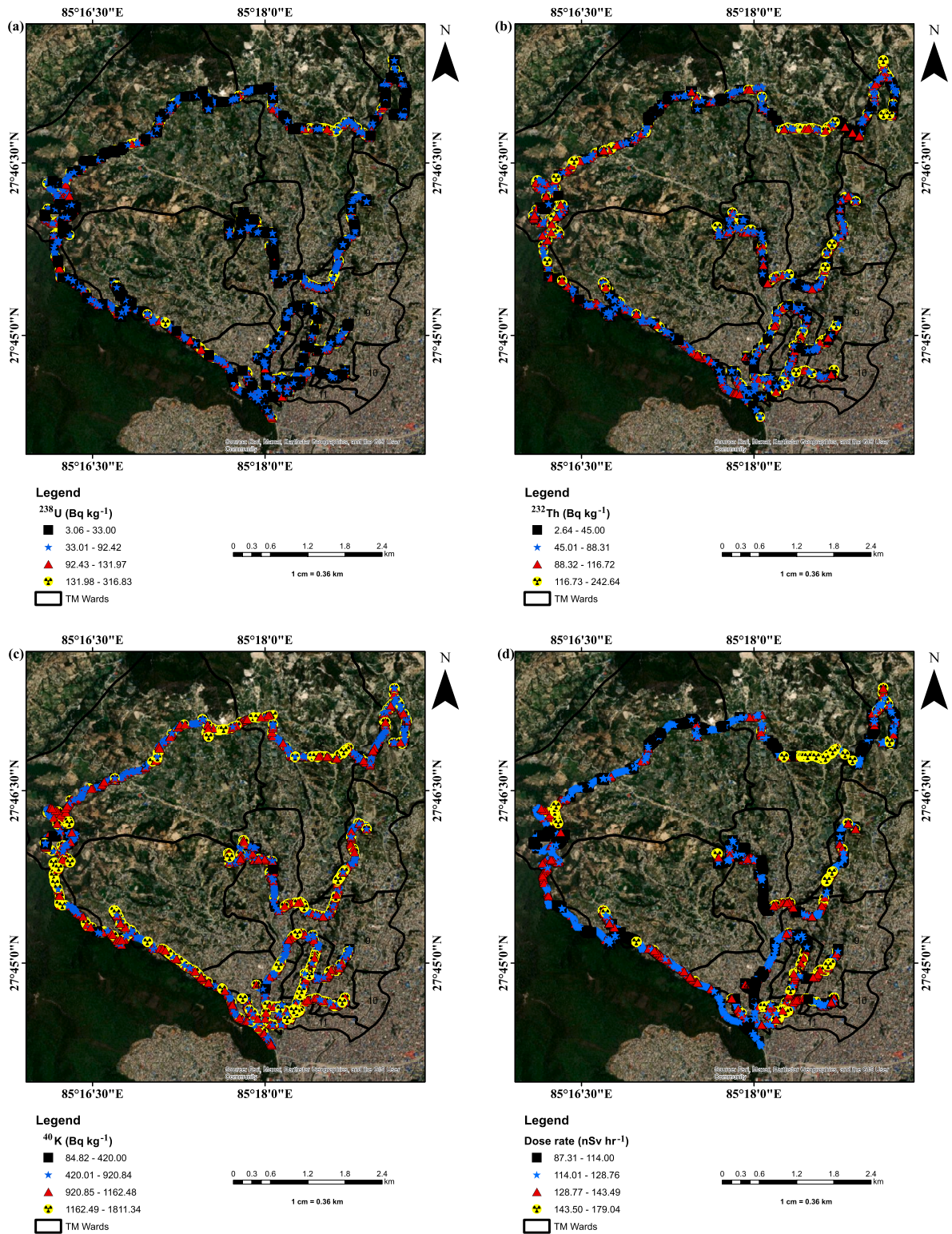
Fig. 7. Base map of study area along with spatial distribution of activity concentration of (a) ^{238}U, (b) ^{232}Th, (c) ^{40}K and (d) Gamma dose rate (nSv hr^{-1}).

Table 5
Comparison of hazard indices with different part of world.

Particulars	$ELCR_I$ 10^{-3}	$AGDE$ μSv yr^{-1}	H_{in}	H_{ex}	I_γ	I_α	RLI	AUI	References
Poland	-	-	-	-	-	-	-	-	[41]
Nepal	-	-	-	-	-	-	-	-	[8]
Nigeria	-	-	-	0.36	-	-	-	-	[45]
Nigeria	-	-	0.67	0.28	-	-	-	-	[16]
Korea	-	-	-	-	-	-	-	-	[24]
Kenya	-	-	-	-	-	-	-	-	[18]
South Africa	-	-	-	-	-	-	-	-	[43]
Egypt	-	-	2.58 - 18.69	1.35 - 9.42	-	-	-	-	[43]
Soil Iraq	-	189.57	0.19	0.16	-	-	-	0.40	[47]
Himalayan Soil	-	-	1.04	0.85	-	-	-	-	[44]
India Soil	-	-	1.13	0.87	1.15	0.48	-	-	[20]
Orissa, India	-	-	-	-	-	-	-	-	[11]
KMC Soil	0.64	243.28	0.25	0.22	0.29	0.05	-	0.72	[5]
Present work	**1.87**±**0.31**	**785.06**± **132.11**	**0.94**±**0.15**	**0.72**±**0.12**	**0.98**±**0.16**	**0.40**±**0.08**	**1.96**±**0.32**	**1.79**±**0.35**	**TM**
UNSCEAR	0.90	300	1	1	1	1	1	2	[26]

throughout the entire area. The average dose rate across the surveyed area ranged from 70.22 to 163.66 nSv hr^{-1}, with an overall average of 124.65 $\pm$ 20.29 nSv hr^{-1}. This average dose rate surpassed the world average of 59 nSv hr^{-1}, indicating elevated levels of natural radioactivity. Activity concentrations of potassium (^{40}K) ranged from 457.59 to 1380.80 Bq kg^{-1}, with an average of 935.26 $\pm$ 172.30 Bq kg^{-1}. This higher-than-average concentration suggests the suitability of the land for agricultural purposes. Uranium (^{238}U) concentrations ranged from 7.78 to 97.74 Bq kg^{-1}, with an average of 80.47 $\pm$ 15.53 Bq kg^{-1}. Thorium (^{232}Th) concentrations ranged from 12.70 to 114.09 Bq kg^{-1}, with an average of 80.44 $\pm$ 18.58 Bq kg^{-1}. Radiological indices exhibited variations, with Radium Equivalent (Ra_{eq}) ranging from 132.26 to 351.22 Bq kg^{-1}, averaging 267.52 $\pm$ 44.79 Bq kg^{-1}. Annual Gonadal Equivalent Dose ($AGDE$) ranged from 372.61 to 1028.81 μSv yr^{-1}, with an average of 785.06 $\pm$ 132.11 μSv yr^{-1}. Annual Effective Dose Rate for indoor and outdoor environments were higher than the world average, with averages of 0.54 $\pm$ 0.09 mSv yr^{-1} and 0.15 $\pm$ 0.03 mSv yr^{-1}, respectively. Excess Lifetime Cancer Risk ($ELCR$) values for both indoor and outdoor environments exceeded the world average, with averages of 0.54$\times10^{-3}$ $\pm$ 0.09$\times10^{-3}$ and 1.87$\times10^{-3}$ $\pm$ 0.31$\times10^{-3}$, respectively. External Hazard Indices (H_{ex}) ranged from 0.36 to 0.59, with an average of 0.72 $\pm$ 0.12. Internal Hazard Indices (H_{in}) ranged from 0.38 to 1.20, with a mean of 0.94 $\pm$ 0.16. The study underscores the need for further analysis using ex-situ equipment such as NaI(Tl), HPGe, or LaBr$_2$ detectors. The obtained data serves as valuable baseline information for future environmental monitoring and assessment efforts, contributing to the development of regulatory frameworks. The elevated radiation levels emphasize the importance of continued scrutiny and management of potential health risks in the surveyed region.

CRediT authorship contribution statement

Devendra Raj Upadhyay: Writing – review & editing, Writing – original draft, Visualization, Validation, Software, Resources, Project administration, Methodology, Investigation, Funding acquisition, Formal analysis, Data curation, Conceptualization. **Anish Phuyal:** Visualization, Investigation, Data curation. **Suffian Mohamad Tajudin:** Writing – review & editing, Visualization. **Raju Khanal:** Writing – review & editing, Supervision, Resources, Conceptualization.

Declaration of competing interest

No known competing financial interests and conflicts of interest exist in relation to the research work presented in this study.

Data availability

Data will be made available on request with suitable reason.

Acknowledgements

References

[1] S.S. Guide, Radiation protection and safety in medical uses of ionizing radiation, in: Specific Safety Guide SSG-46, IAEA, Vienna, 2018.

[2] C. Bajwa, R. Pope, L. Baekelandt, Y. Zhao, D. Mennerdahl, Developing historical technical basis for radiological safety requirements of international transport safety regulations, Packag. Transp. Storage Secur. Radioact. Mater. 24 (4) (2013) 213–219.

[3] V. Beir, Health effects of exposure to low levels of ionizing radiation, in: Biological Effects of Ionizing Radiations, 1990, pp. 22–45.

[4] M. Eisenbud, T.F. Gesell, Environmental Radioactivity from Natural, Industrial and Military Sources, Elsevier, 1997.

[5] D.R. Upadhyay, G. Koirala, B.R. Shah, S.M. Tajudin, R. Khanal, Assessing radioactive contaminants in Kathmandu soils: measurement and risk analysis, Environ. Monit. Assess. 196 (2) (2024) 190, https://doi.org/10.1007/s10661-023-12284-5.

[6] G. Wallova, K. Acharya, G. Wallner, Determination of naturally occurring radionuclides in selected rocks from Hetaunda area, central Nepal, J. Radioanal. Nucl. Chem. 283 (3) (2010) 713–718, https://doi.org/10.1007/s10967-009-0401-3.

[7] A. Mishra, R. Khanal, Outdoor effective dose and associated health risk in the premises of Tribhuvan University in-situ gamma ray spectrometry, Himal. Phys. 8 (2019) 47–52, https://doi.org/10.3126/hp.v8i0.30001.

[8] A. Mishra, R. Khanal, In-situ radiometric assessment of UNESCO World Heritage sites in Kathmandu Valley of Nepal using gamma ray spectrometry, Jordan J. Phys. 16 (2) (2023) 215–227, https://doi.org/10.47011/16.2.9.

[9] M. Ghiassi-Nejad, S. Mortazavi, J. Cameron, A. Niroomand-Rad, P. Karam, Very high background radiation areas of Ramsar, Iran: preliminary biological studies, Health Phys. 82 (1) (2002) 87–93, https://doi.org/10.1097/00004032-200201000-00011.

[10] M. Barcinski, M.D.C. Abreu, J. De Almeida, J. Naya, L. Fonseca, L. Castro, Cytogenetic investigation in a Brazilian population living in an area of high natural radioactivity, Am. J. Hum. Genet. 27 (6) (1975) 802.

[11] A. Mohanty, D. Sengupta, S. Das, V. Vijayan, S. Saha, Natural radioactivity in the newly discovered high background radiation area on the eastern coast of Orissa, India, Radiat. Meas. 38 (2) (2004) 153–165, https://doi.org/10.1016/j.radmeas.2003.08.003.

[12] M. Chougaonkar, K. Eappen, T. Ramachandran, P. Shetty, Y. Mayya, S. Sadasivan, V. Venkat Raj, Profiles of doses to the population living in the high background radiation areas in Kerala, India, J. Environ. Radioact. 71 (3) (2004) 275–297, https://doi.org/10.1016/S0265-931X(03)00174-7.

[13] T. Jiang, I. Hayata, C. Wang, S. Nakai, S. Yao, Y. Yuan, L. Dai, Q. Liu, D. Chen, L. Wei, et al., Dose-effect relationship of dicentric and ring chromosomes in lymphocytes of individuals living in the high background radiation areas in China, J. Radiat. Res. 41 (SUPPL) (2000) S63–S68, https://doi.org/10.1269/jrr.41.S63.

[14] A.S. Aliyu, A.T. Ramli, The world's high background natural radiation areas (HBNRAs) revisited: a broad overview of the dosimetric, epidemiological and radiobiological issues, Radiat. Meas. 73 (2015) 51–59, https://doi.org/10.1016/j.radmeas.2015.01.007.

[15] J. Ondieki, C. Mito, M. Kaniu, Feasibility of mapping radioactive minerals in high background radiation areas using remote sensing techniques, Int. J. Appl. Earth Obs. Geoinf. 107 (2022) 102700, https://doi.org/10.1016/j.jag.2022.102700.

[16] E. Joel, M. Omeje, O. Olawole, G. Adeyemi, A. Akinpelu, Z. Embong, M. Saeed, In-situ assessment of natural terrestrial-radioactivity from Uranium-238 (^{238}U), Thorium-232 (^{232}Th) and Potassium-40 (^{40}K) in coastal urban-environment and its possible health implications, Sci. Rep. 11 (1) (2021) 1–14, https://doi.org/10.1038/s41598-021-96516-z.

[17] M. Kaniu, I. Darby, H. Angeyo, Assessment and mapping of the high background radiation anomaly associated with laterite utilization in the south coastal region of Kenya, J. Afr. Earth Sci. 160 (2019) 103606, https://doi.org/10.1016/j.jafrearsci.2019.103606.

[18] M. Kaniu, H. Angeyo, I. Darby, L. Muia, Rapid in-situ radiometric assessment of the Mrima-Kiruku high background radiation anomaly complex of Kenya, J. Environ. Radioact. 188 (2018) 47–57, https://doi.org/10.1016/j.jenvrad.2017.10.014.

[19] M.K. Nair, K. Nambi, N.S. Amma, P. Gangadharan, P. Jayalekshmi, S. Jayadevan, V. Cherian, K.N. Reghuram, Population study in the high natural background radiation area in Kerala, India, Radiat. Res. 152 (6s) (1999) S145–S148, https://doi.org/10.2307/3580134.

[20] M. Prasad, V. Ranga, G.A. Kumar, R. Ramola, Radiological impact assessment of soil and groundwater of Himalayan regions in Uttarakhand, India, J. Radioanal. Nucl. Chem. 323 (2020) 1269–1282, https://doi.org/10.1007/s10967-019-06827-9.

[21] NSO, National Population and Housing Census 2021: population size and distribution, https://censusnepal.cbs.gov.np/results/population?province=3&district=28&municipality=6. (Accessed 22 May 2023), 2021.

[22] J. Elliott, R. Jolivet, P.J. González, J.-P. Avouac, J. Hollingsworth, M. Searle, V. Stevens, Himalayan megathrust geometry and relation to topography revealed by the Gorkha earthquake, Nat. Geosci. 9 (2) (2016) 174–180, https://doi.org/10.1038/ngeo2623.

[23] IAEA, Construction and use of calibration facilities for radiometric field equipment, https://inis.iaea.org/collection/NCLCollectionStore/_Public/21/028/21028964.pdf. (Accessed 10 February 2024), 1989.

[24] N. Hassan, Y. Kim, J. Jang, B. Chang, J. Chae, Comparative study of precise measurements of natural radionuclides and radiation dose using in-situ and laboratory γ-ray spectroscopy techniques, Sci. Rep. 8 (1) (2018) 14115, https://doi.org/10.1038/s41598-018-32220-9.

[25] IAEA, Guidelines for radioelement mapping using gamma ray spectrometry data, https://www-pub.iaea.org/MTCD/Publications/PDF/te_1363_web.pdf. (Accessed 5 February 2024), 2003.

[26] UNSCEAR, Sources and Effects of Ionizing Radiation, United Nations Scientific Committee on the Effects of Atomic Radiation (UNSCEAR) 2000 Report, Volume I: Report to the General Assembly, with Scientific Annexes-Sources, United Nations, 2000.

[27] X. Liu, W. Lin, Natural radioactivity in the beach sand and soil along the coastline of Guangxi Province, China, Mar. Pollut. Bull. 135 (2018) 446–450, https://doi.org/10.1016/j.marpolbul.2018.07.057.

[28] K. Inoue, M. Fukushi, T. Le Van, H. Tsuruoka, S. Kasahara, V. Nimelan, Distribution of gamma radiation dose rate related with natural radionuclides in all of Vietnam and radiological risk assessment of the built-up environment, Sci. Rep. 10 (1) (2020) 1–14, https://doi.org/10.1038/s41598-020-69003-0.

[29] C.C. Mbonu, U.C. Ben, Assessment of radiation hazard indices due to natural radioactivity in soil samples from Orlu, Imo State, Nigeria, Heliyon 7 (8) (2021), https://doi.org/10.1016/j.heliyon.2021.e07812.

[30] A. Kurnaz, B. Küçükömeroğlu, R. Keser, N. Okumusoglu, F. Korkmaz, G. Karahan, U. Çevik, Determination of radioactivity levels and hazards of soil and sediment samples in Fırtına Valley (Rize, Turkey), Appl. Radiat. Isot. 65 (11) (2007) 1281–1289, https://doi.org/10.1016/j.apradiso.2007.06.001.

[31] E. Joel, O. Maxwell, O. Adewoyin, O. Olawole, T. Arijaje, Z. Embong, M. Saeed, Investigation of natural environmental radioactivity concentration in soil of coastaline area of Ado-Odo/Ota Nigeria and its radiological implications, Sci. Rep. 9 (1) (2019) 1–8, https://doi.org/10.1038/s41598-019-40884-0.

[32] S. Şahin Bal, The determination of concentrations of radioisotopes in some granite samples in Turkey and their radiation hazards, Radiat. Eff. Defects Solids 173 (5–6) (2018) 353–366, https://doi.org/10.1080/10420150.2018.1462358.

[33] R. Ravisankar, K. Vanasundari, M. Suganya, Y. Raghu, A. Rajalakshmi, A. Chandrasekaran, S. Sivakumar, J. Chandramohan, P. Vijayagopal, B. Venkatraman, Multivariate statistical analysis of radiological data of building materials used in Tiruvannamalai, Tamilnadu, India, Appl. Radiat. Isot. 85 (2014) 114–127, https://doi.org/10.1016/j.apradiso.2013.12.005.

[34] A. Sam, N. Abbas, Assessment of radioactivity and the associated hazards in local and imported cement types used in Sudan, Radiat. Prot. Dosim. 93 (3) (2001) 275–277, https://doi.org/10.1093/oxfordjournals.rpd.a006440.

[35] M.F. Attallah, H.M. Abdelbary, E.A. Elsofany, Y.T. Mohamed, M.M. Abo-Aly, Radiation safety and environmental impact assessment of sludge TENORM waste produced from petroleum industry in Egypt, Process Saf. Environ. Prot. 142 (2020) 308–316, https://doi.org/10.1016/j.psep.2020.06.012.

[36] R. Ravisankar, Y. Raghu, A. Chandrasekaran, M.S. Gandhi, P. Vijayagopal, B. Venkatraman, Determination of natural radioactivity and the associated radiation hazards in building materials used in Polur, Tiruvannamalai District, Tamilnadu, India using gamma ray spectrometry with statistical approach, J. Geochem. Explor. 163 (2016) 41–52, https://doi.org/10.1016/j.gexplo.2016.01.013.

[37] ICRP, Recommendations of the international commission on radiological protection. ICRP publication 60, Ann. ICRP 21 (1991) 1–3, https://journals.sagepub.com/doi/pdf/10.1177/ANIB_21_1-3.

[38] O. Belyaeva, N. Movsisyan, K. Pyuskyulyan, L. Sahakyan, G. Tepanosyan, A. Saghatelyan, Yerevan soil radioactivity: radiological and geochemical assessment, Chemosphere 265 (2021) 129173, https://doi.org/10.1016/j.chemosphere.2020.129173.

[39] S. Suresh, D. Rangaswamy, J. Sannappa, S. Dongre, E. Srinivasa, S. Rajesh, Estimation of natural radioactivity and assessment of radiation hazard indices in soil samples of Uttara Kannada district, Karnataka, India, J. Radioanal. Nucl. Chem. 331 (4) (2022) 1869–1879, https://doi.org/10.1007/s10967-021-08145-5.

[40] M. Momčilović, J. Kovačević, M. Tanić, M. Đorđević, G. Bačić, S. Dragović, Distribution of natural radionuclides in surface soils in the vicinity of abandoned uranium mines in Serbia, Environ. Monit. Assess. 185 (2013) 1319–1329, https://doi.org/10.1007/s10661-012-2634-9.

[41] D. Tchorz-Trzeciakiewicz, B. Kozłowska, A. Walencik-Łata, Seasonal variations of terrestrial gamma dose, natural radionuclides and human health, Chemosphere 310 (2023) 136908, https://doi.org/10.1016/j.chemosphere.2022.136908.

[42] S. Ghias, K.H. Satti, M. Khan, M. Dilband, A. Naseem, A. Jabbar, S. Kali, T. Ur-Rehman, J. Nawab, M. Aqeel, M.A. Khan, M.I. Zafar, Health risk assessment of radioactive footprints of the urban soils in the residents of Dera Ghazi Khan, Pakistan, Chemosphere 267 (2021) 129171, https://doi.org/10.1016/j.chemosphere.2020.129171.

[43] J. Bezuidenhout, In situ gamma ray measurements of radionuclides at a disused phosphate mine on the West Coast of South Africa, J. Environ. Radioact. 150 (2015) 1–8, https://doi.org/10.1016/j.jenvrad.2015.07.030.

[44] A. Kumar, P. Singh, P. Semwal, K. Singh, M. Prasad, R.C. Ramola, Study of primordial radionuclides and radon/thoron exhalation rates in Bageshwar region of Kumaun Himalaya, India, J. Radioanal. Nucl. Chem. 328 (2021) 1361–1367, https://doi.org/10.1007/s10967-020-07582-y.

[45] O. Adewoyin, O. Maxwell, S. Akinwumi, T. Adagunodo, Z. Embong, M. Saeed, Estimation of activity concentrations of radionuclides and their hazard indices in coastal plain sand region of Ogun state, Sci. Rep. 12 (1) (2022) 1–8, https://doi.org/10.1038/s41598-022-06064-3.

[46] I. Gaafar, M. Hanfi, L.S. El-Ahll, I. Zeidan, Assessment of radiation hazards from phosphate rocks, Sibaiya area, central eastern desert, Egypt, Appl. Radiat. Isot. 173 (2021) 109734, https://doi.org/10.1016/j.apradiso.2021.109734.

[47] T.Y. Wais, F.N.M. Ali, L.A. Najam, H. Mansour, M.Y.A. Mostafa, Assessment of natural radioactivity and radiological hazards of soil collected from Rabia town in Nineveh Governorate (North Iraq), Phys. Scr. 98 (6) (2023) 065304, https://doi.org/10.1088/1402-4896/acd732.